Solid Freeform Fabrication 2021: Proceedings of the 32nd Annual International
Solid Freeform Fabrication Symposium – An Additive Manufacturing Conference
Reviewed Paper

Challenges during laser powder bed fusion of a near-alpha titanium alloy - Ti-6242Si

Sagar Patel[1], Mohsen Keshavarz[1], Mihaela Vlasea[1*]

[1]Department of Mechanical and Mechatronics Engineering, University of Waterloo, Waterloo, ON N2L 3G1, Canada

[*]Corresponding author: mihaela.vlasea@uwaterloo.ca

Abstract

Ti-6Al-2Sn-4Zr-2Mo-Si (Ti-6242Si) is a near-α phase titanium alloy that has a greater strength up to 565 °C compared to the workhorse Ti-6Al-4V alloy with a typical service temperature of up to 400 °C. While there is a wealth of literature to help understand the laser powder bed fusion (LPBF) of Ti-6Al-4V, only a few research articles about LPBF of Ti-6242Si are available in the open literature. In this work, LPBF processing diagrams and temperature prediction models were used to investigate the impact of process parameters such as laser power, scan speed, and beam spot radius on macroscale characteristics of the builds such as density and surface roughness. The use of processing diagrams allowed for exploration of density ranges between 99.55-99.98 %, and surface roughness, *Sa*, ranges between 8-16 μm in Ti-6242Si processed by LPBF. Cracking in Ti-6242Si manufactured by LPBF is reported for the first time. Cracking during LPBF of Ti-6242Si was observed to strongly depend upon the predicted melting mode (conduction, transition, and keyhole) for a given set of LPBF process parameters.

KEYWORDS: Laser powder bed fusion, selective laser melting, titanium, Ti6242, density, roughness, cracking

Introduction

Laser powder bed fusion (LPBF) is a metal additive manufacturing (AM) technology that alongside electron beam melting (EBM) has the highest industrial uptake at the moment in the aerospace, automotive, and biomedical sectors [1]. LPBF enables the manufacturing of near net-shape geometrically complex parts. LPBF allows for optimized designs to be explored for manufacturing, such as topology optimized or loading field driven designs for product lightweighting and customization [2], while also reducing environmental impact through input energy reduction and carbon dioxide emissions [3]. The potential of LPBF to build lightweight components has been shown to improve fuel consumption for aerospace and automotive applications, wherein titanium alloys are commonly used [4,5].

While additively manufactured titanium alloys are already used for industrial applications in the aerospace [6–8] and biomedical sectors [9–12], the low number of additive manufactured titanium alloys available reduce their potential applications [5]. From the available titanium alloys, the $\alpha + \beta$ alloy Ti-6Al-4V (Ti64) is known as the "workhorse" titanium alloy represents almost half of the total usage of titanium alloys for aerospace applications [6]. When compared to Ti64, the near-α Ti-6Al-2Sn-4Zr-2Mo-Si (Ti-6242Si) is known to have improved mechanical properties, particularly creep behaviour [5], which is useful for applications such as high-pressure compressor parts in aviation engines [13]. Alpha (α) and near-α Ti alloys are commonly used in applications where higher strength and toughness, excellent creep resistance, and stress stability is desired at higher working temperatures up to 600°C when compared to Ti64 that cannot be used beyond a service temperate of 400°C [14]. Ti-6242Si, in particular, has been recommended for high temperature applications of up to 565°C [15]. The nominal chemical composition of Ti-6242Si by weight percent (wt%) is: 6 Al, 2 Sn, 4 Zr, 2 Mo, 0.08 Si, 0.05 N, 0.05 C, 0.0125 H, 0.25 Fe, 0.15 O, and balance Ti [16]. Ti-6242Si has also been proposed to be better suited for certain superconductivity applications when compared to Ti64 [17].

A survey of open literature shows that LPBF of Ti-6242Si has been investigated by two groups of researchers till date. Fan and Yang [18] reported a successful use of LPBF to manufacture Ti-6242Si cubic and tensile samples for the first time. Density values of 95.7%-99.5%, hardness of 410 HV, ultimate tensile strength (UTS) of 1437 MPa, and ductility of 5% were reported for the as-built Ti-6242Si samples. A hardness of 450 HV, UTS of 1510 MPa, and ductility of 1.4% were reported for the Ti-6242Si samples aged at 595 °C for 8 hours. Rieger et al. [5] reported improved mechanical properties of LPBF Ti-6242Si at both room and elevated temperatures (500 °C) when compared to LPBF Ti64 and conventionally cast Ti-6242Si. A non-equilibrium hexagonal α' martensitic microstructure was reported for both Ti-6242Si and Ti64 in as-built condition as is generally observed due to the high cooling rates (1–40K/µs) associated with LPBF [19]. While using the same LPBF process parameters, Rieger et al. [5] reported smaller acicular α' grains in Ti-6242Si compared to Ti64, which were attributed to the smaller prior β grain structure in Ti-6242Si. Nonetheless, cracking during LPBF of Ti-6242Si was not reported in either of these articles.

This work is the first attempt at spanning all three melting modes during LPBF of Ti-6242Si, thereby testing the limits of processing this near- α alloy by LPBF. This work focuses on using normalized processing diagrams developed in prior work [20] to investigate the influence of LPBF process parameters on density, side-skin surface roughness, and cracking during LPBF of Ti-6242Si. Laser power, scan speed, and beam spot radius are the principal LPBF process parameters considered for this work.

Materials and Methods

Two sets of samples were manufactured in the same build: cylindrical and cuboid samples. 12 cylindrical Ti6242 coupons with a diameter of 10 mm and a height of 30 mm, and 9 cuboids of 5x5x10 mm^3 were manufactured on the reduced build volume (RBV) of a modulated Renishaw AM 400 LPBF system. The cylinders were used to optimize the process parameters of the core of the samples targeting the density, and cuboids were manufactured with the purposes of optimizing process parameters to obtain low side-skin surface roughness. The Ti6242 powders obtained from AP&C were plasma atomized, with a particle size range of 15–45 µm (D10 of 20 µm, D50 of 34 µm, and D90 of 44 µm). A constant powder layer thickness of 30 µm was used for all samples. The build plate layout of the parts with respect to the gas flow and powder flow is shown in Figure 1.

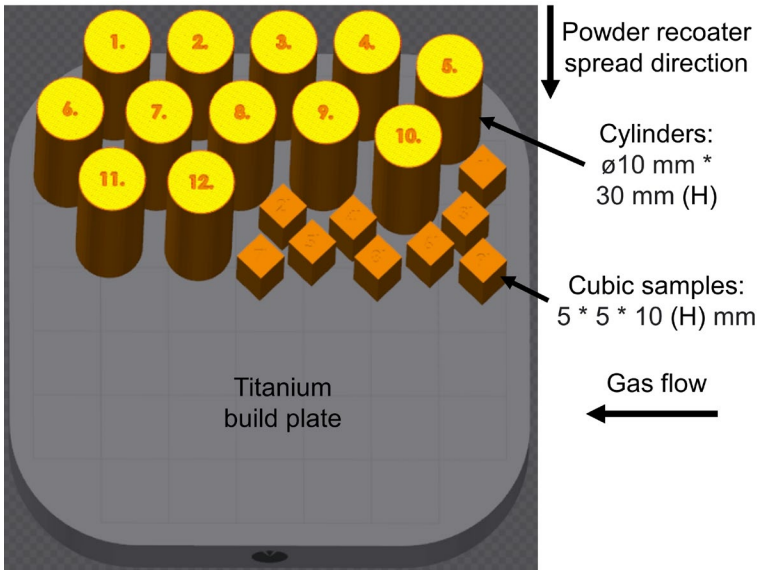

Figure 1. Illustration of the build plate layout on the reduced build volume of the Renishaw AM 400 for the manufactured Ti-6242Si cylinders and cubic samples showing the powder flow direction and argon gas flow.

LPBF process parameters such as laser power, scan speed (by means of exposure time), and beam spot radius are known to be the variables that have the highest impact on driving the presence of conduction, transition, or keyhole melting modes [20]. This motivated the LPBF process parameter selection for the core of

the 12 cylinders shown in Table 1. A hatch distance equal to the beam diameter was chosen for a given cylinder to minimize the potential for lack of fusion defects.

The LPBF process parameters that were varied for the cylinders (for density evaluation) are shown in Table 1. The point distance was kept constant at 55 μm for all cylinders. The beam spot radius variations were obtained by defocusing the beam to positions above the build as illustrated in Fig. 2 of Ref. [21]. Renishaw AM 400 provides a laser beam wavelength of λ = 1070 nm, and the beam spot radius at the focal point is $r_0 = 35$ μm. The laser beam was defocused to two distances (z) of 3.67 and 5.63 mm above the build plate, to obtain divergent beams of radiuses 50 and 65 μm, respectively, as shown in Table 1. These values were calculated for a Gaussian distribution by equation (1). For both cylinders and cuboids, the scanning strategy included scanning of the hatch volume (core) using the meander scanning strategy, followed by a border scan that involves melting of the edge of each layer of a coupon. The direction of core meander scanning was rotated by 67° between successive layers. For the cylinders, the border parameters were kept constant with power – 100 W, point distance – 45 μm, and exposure time – 40 μs.

$$r = r_0 \left[1 + \left(\frac{z\lambda}{\pi r_o^2} \right)^2 \right]^{1/2} \quad (1)$$

Table 1. LPBF process parameters used in the core of the Ti-6242Si cylinders – density evaluation. Border parameters were kept constant for all cylinders.

Sample code	Power (W)	Exposure time (μs)	Beam spot radius (μm)	Hatch distance (μm)
1	225	30	50	100
2	150	30	35	70
3	300	30	65	130
4	375	30	65	130
5	150	50	35	70
6	300	50	50	100
7	375	50	65	130
8	225	50	35	70
9	300	50	65	130
10	225	50	50	100
11	300	30	50	100
12	225	30	35	70

In the cuboids, the core was kept constant at the process parameters used for cylindrical sample 10 from Table 1 but the parameters for the border scan were varied as shown in Table 2 with a laser power 225 W, point distance 55 μm, exposure time 50 μs, beam radius 50 μm, and hatch distance 100 μm. In these samples, the point distance was kept constant at 55 μm, and the beam spot radius was 35 μm (focused beam) for the borders.

Table 2. LPBF process parameters used in the borders of the Ti-6242Si cuboids – side-skin surface roughness evaluation. The point distance was kept constant at 55 μm, and the beam spot radius was 35 μm (focused beam). Core parameters were kept constant for all cuboids.

Sample code	Power (W)	Exposure time (μs)
A	100	25

B	250	45
C	100	45
D	100	65
E	175	45
F	175	25
G	250	25
H	250	45
I	250	65

X-ray computed tomography (XCT) methods

The manufactured cylinders were removed off the build plate by electrical discharge machining (EDM) and analyzed for porosity characteristics using a 3D X-ray computed tomography (CT) scanner (ZEISS Xradia 520 Versa) using a 11 μm voxel size. The X-ray CT scanning parameters used are shown in Table 3. To visualize the pore distribution within each sample, the CT scans were analyzed using an image processing software (Dragonfly 3.0, Object Research Systems Inc.). The brightness, contrast, and opacity of the data volume were adjusted to highlight the features of interest within the CT scans. For each cylinder, the entire diameter of 10 mm and approximately 8.5 mm of height along the build (Z) direction, along the central region of the cylinders was analyzed. Cylinders 6 and 8 from Table 1 and Figure 2 cracked on the build plate before the EDM cut. Due to the multiple cracks on the samples that were perpendicular to the build direction, it was not possible to evaluate 8.5 mm height for density. A diameter of 10 mm and approximately 7.2 mm of height for cylinders 6 and 8 was hence evaluated.

Table 3. X-ray computed tomography parameters used for scanning the Ti-6242Si cylinders.

Parameter	Unit	Value
Voxel size	[μm]	11
Source power	[W]	10
X-ray energy	[kV]	140
Filter	-	HE2
X-ray optic	-	0.4× lens
Source position	[mm]	23.1391
Detector position	[mm]	120.787
Exposure time	[s]	2.0
Number of projections	-	1001
Binning level	-	2

Microscopy and imaging methods

The surface topography of the side-skin surfaces of the cuboid samples from Table 2 and Figure 3 was characterized using the Keyence VK-X250, a laser confocal microscope. The image processing and roughness measurements were completed using the microscopes processing software. A scanning area of approximately 700x500 μm^2 was scanned on the 4 side-skin surfaces (surface along the build (Z) direction) of each cuboid, using a vertical z-axis resolution of 0.5 μm. *Sa* and *Sz* are the surface roughness metrics used in this work. *Sa* is the arithmetical mean height of a surface area which is defined as the absolute value of the height from the average surface. *Sz* is the sum of the largest peak height value and the largest pit depth value within a scanned area of a given surface. Surface correction for plane tilt was employed for all scans, to accommodate for the tilt cause by the roughness of the resting surface. The roughness is measured near the middle of the sample height

i.e., approximately halfway through the build height of the sample for all 4 surfaces of each sample. Measurements of *Sa* and *Sz* from the 4 surfaces of every cuboid were used to calculate the average and standard deviation values of *Sa* and *Sz* shown in Figure 3. This procedure is similar to the one adopted by Patel et al. [22] and Rogalsky et al. [23].

Results and Discussion

Processing diagrams to identify melting modes

The normalized processing diagrams for the Ti-6242Si cylinders shown in Figure 2 and Figure 3 are obtained through the methodology described in previous work [20]. The terms E^* and v^* in Figure 2 are given by equation (2) and (3), respectively.

$$E^* = \frac{q^*}{l^*} = \frac{AP_{eff}}{2l_t\lambda(T_m - T_0)} \tag{2}$$

$$v^* = \frac{vr_B}{\alpha} \tag{3}$$

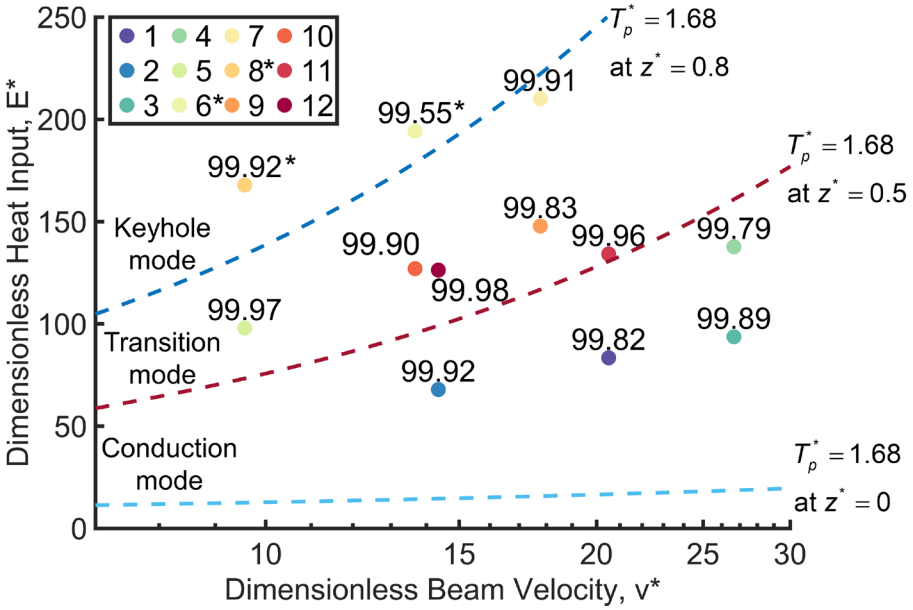

Figure 2. Normalized processing diagrams for the twelve Ti-6242Si cylinders used for density evaluation. The density values obtained from XCT data in percentage (%) are provided next to the points on the diagram. The cracked samples are shown by an asterisk sign (*) next to their labels and density values.

In equation (2), E^* is dimensionless heat input, P_{eff} is the effective laser power [W], A is laser absorptivity, l_t is powder layer thickness [m], λ is thermal conductivity [W/(m.K)], T_m is melting temperature [K], and T_0 is initial (or powder bed) temperature [K]. In equation (3), v^* is dimensionless beam velocity, v is the laser beam velocity [m/s], r_b is beam spot radius [m], and α is thermal diffusivity [m^2/s]. Values for the Ti6242 material constants are taken at the room temperature from Welsch et al. [15] and are summarized in Table 4. The dimensionless beam power term, q^*, and the dimensionless layer thickness term, l^*, are defined in equations (4) and (5) respectively [24,25].

$$q^* = \frac{AP}{r_B\lambda(T_m - T_0)} \tag{4}$$

$$l^* = \frac{2 \cdot l_t}{r_B} \tag{5}$$

The laser absorptivity, A, values chosen for a given set of process parameters in equation (2) are obtained from equation (6), which is an adaptation of the scaling law for laser absorptivity determined by Ye et al. [26] for low reflectivity Ti, Fe, and Ni alloys using the terms derived in [20].

$$A = 0.70\left(1 - \exp\frac{-0.66 q_m^*}{\pi v^*}\right) \tag{6}$$

The term, q_m^*, in equation (6) is obtained by replacing the A term in equation (4) with A_m (the minimum melt absorptivity). The minimum melt absorptivity, A_m, value for titanium alloys is reported as 0.26 by Ye et al. [26] which is used in this work.

Table 4. Thermophysical properties of Ti-6242Si used in this work [15].

Properties	Material (Ti-6242Si)
Density [kg/m^3]	4540
Thermal conductivity [W/m.K]	7
Specific heat capacity [J/kg.K]	460
Melting temperature [K]	1978
Vaporization temperature [K]	3315

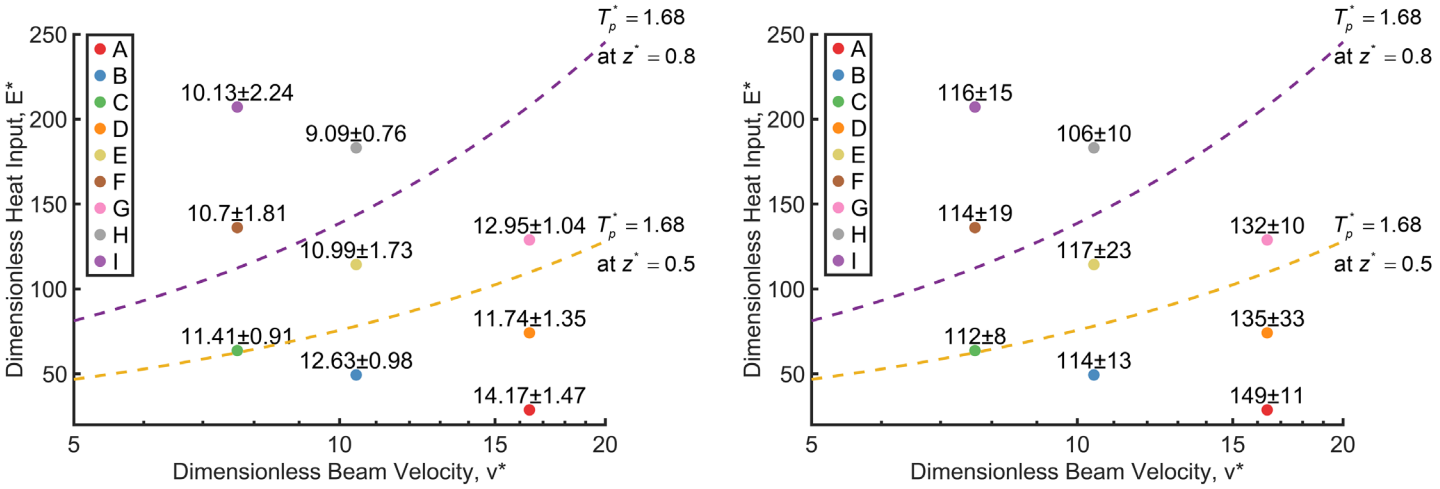

Figure 3. Normalized processing diagrams for the nine Ti-6242Si cubic samples used for side-skin surface roughness evaluation with the Sa values in µm (left) and Sz values in µm (right).

The effective laser power, P_{eff}, for modulated LPBF systems such as the Renishaw AM 400 is given by equation (7). Additionally, equation (8) is used to obtain the values for laser beam velocity, v, in this work.

$$P_{eff} = \frac{P \cdot t_e}{t_e + t_d} \tag{7}$$

$$v = \frac{p_d}{t_e + t_d} \tag{8}$$

In equations (1.3) and (8), t_e is the time when the laser is acting on the material (exposure time) [s], and t_d is the time when the laser is off and repositioning to the next exposure point (drill delay time) - assumed to be 10 μs for the AM 400 system. In equation (8), p_d is the distance between adjacent exposure points (point distance) [μm]. The dimensionless peak temperature, T_p^*, in the melt pool used for predicting the melting mode thresholds is derived in previous work [20]. For low reflectivity materials such as titanium, the threshold between conduction mode and transition mode is predicted to be when the vaporization depth exceeds 0.5 times beam spot radius used, i.e., $T_p^* = 1.68$ at $z^* = 0.5$, where 1.68 is the ratio of the boiling point (vaporization temperature) of Ti-6242Si and its melting point. The term z^* is dimensionless depth given by the ratio of the dimension along the depth of a melt pool, z and the beam spot radius, r_b. The term $z^* = 0.5$ corresponds to a vaporization depth, $d_v = 0.5r_b$, i.e., a vaporization depth equal to half the beam radius used. Similarly, the threshold between transition mode and keyhole mode is predicted to be when the vaporization depth exceeds 0.8 times the beam spot radius used, i.e., $T_p^* = 1.68$ at $z^* = 0.8$, as shown in Figure 2 and Figure 3 [20].

Pore space and cracking characteristics

The normalized processing diagrams for the density study are shown in Figure 2 which help to predict the melting mode for a given set of LPBF process parameters, thereby enabling an understanding of the physical origin of porous defects in the three-dimensional cylinders. Density values for each cylinder were obtained from the XCT data which are shown next to each cylinder's marker in Figure 2. It is important to note that the density values obtained from XCT are approximations of the true density and a relative assessment of part quality due to the voxel size (11 μm) detection limit. A lower voxel size would help in detecting finer defects and could thereby lead to lower density values for the samples. Nonetheless, Ti-6242Si seems to have a wide-processing window for near fully dense parts as cylinders with over 99.90% density are observed in the conduction mode (cylinder 2), transition mode (cylinders 5, 7, 10, 11, and 12), and keyhole mode (cylinder 8). In Figure 4 and Figure 5, defects with aspect ratios above 0.7 were considered as rounded defects and defects below this aspect ratio were considered as irregularly shaped defects. More description of the porous defect visualization can be found in our prior work [21].

An orthographic projection of the porous defect space for 6 representative cylinders along with build plate (XY) plane is shown in Figure 4. In the keyhole mode cylinders (#6 and 8), a length of approximately 7.2 mm in the region between the 2 cracks as shown in Figure 6 were used for the porous defect visualization in Figure 4. All 6 samples in Figure 4 show a higher concentration of porous defects near the sidewalls of the cylinders. These porous defects are caused by the rapid formation and collapse of deep vaporized regions due to the lower laser beam velocity at the turn points of a given layer which is common across most LPBF systems [27]. The collapse of the vaporized regions of the melt pools leads to trapping of atmospheric gases in the solidified parts, which was argon in this work. The processing diagram for the cylinders in Figure 2 shows that all the samples (including the conduction mode samples) lie above the predicted surface vaporization threshold which is given by $T_p^* = 1.68$ at $z^* = 0$ for Ti-6242Si. Hence the presence of vaporization related defects near the sidewalls of all cylinders matches the predictions from the processing diagrams. Additionally, most of the defects near the sidewalls of the cylinders seem to have an irregular morphology as shown in Figure 4. It is known that defects which form due to material vaporization instabilities may have both rounded and irregularly-shaped morphologies; and defects due to collapse of the vaporized region in particular are known to have irregularly-shaped morphologies [20,28].

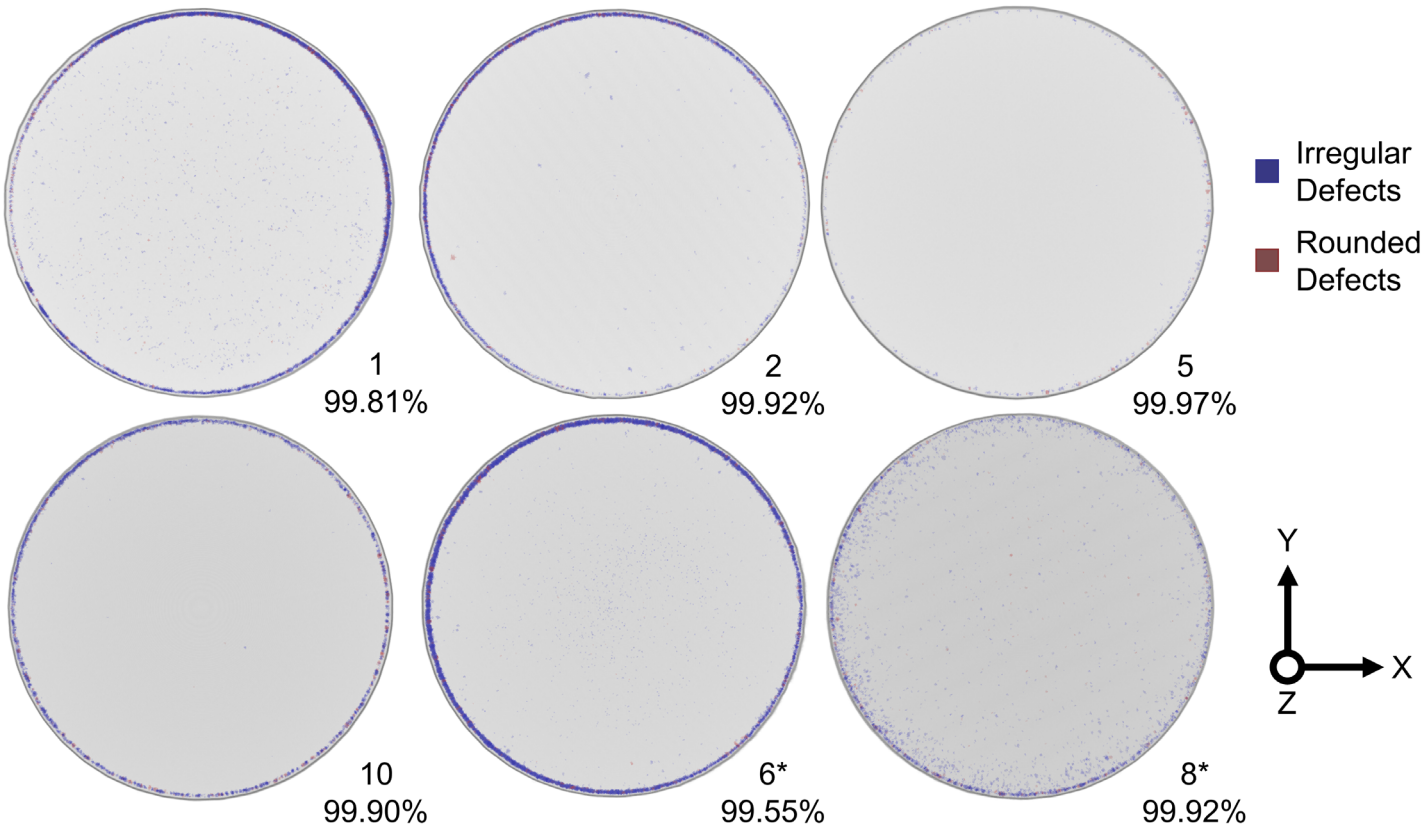

Figure 4. An orthographic projection of the porous defect space (above 4 voxels) in the build plate (XY) plane from the XCT data of conduction mode cylinders (1, 2), transition mode cylinders (5, 10), and keyhole mode cylinders (6, 8). The percentage values provided next to the cylinder labels are the density values also represented in Figure 2.

The absence of large irregular lack of fusion defects in Figure 4 and Figure 5 indicates that the melt pool stitching caused by the selection of hatch distance and powder layer thickness was appropriate for the given sets of process parameters. The processing window for near-fully dense Ti-6242Si parts by LPBF on the Renishaw AM 400 seems to be particularly focused in the transition melting mode as observed by cylinders 5, 7, 10, 11, and 12 with densities over 99.90% in Figure 2. Amongst the 6 cylinders visualized in Figure 4, cylinder 5 seems to have the highest density of 99.97%. A three-dimensional visualization of the porous defects space distribution in cylinder 5 along the build (Z) direction is shown in Figure 5 which confirms the presence of very few defects along only the sidewalls of the cylinder. The absence of rounded vaporization instability related defects in the two keyhole mode cylinders 6 and 8 in Figure 4 means that the LPBF process parameters selected for the samples were likely not aggressive enough to cause such defects. Similar to Ti64 (Ti64), Ti-6242Si is expected to form a dominant martensitic microstructure in LPBF [5,18]. Literature suggests a broad processing window across the three melting modes for such materials [29–33], which is the outcome that is observed through this evaluation of melting modes on density of LPBF Ti-6242Si. Additionally, since it is not possible to observe melt pools in three-dimensional components made out of martensitic titanium alloys such as Ti64 [34], the use of normalized processing diagrams alongside non-destructive characterization equipment such as XCT is an efficient method to rapidly develop process parameters for similarly martensitic materials such as Ti-6242Si.

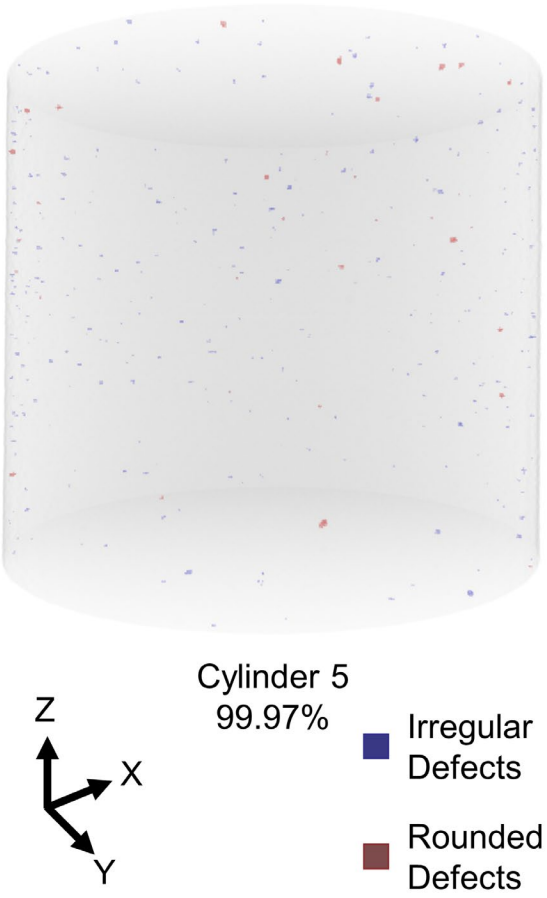

Figure 5. A three-dimensional visualization of the porous defect space (above 4 voxels) along the build direction (Z) from the XCT data of cylinder 5 (highest density), along with the density value obtained from the XCT data.

While cylinders 6 and 8 had a high density in the XCT results shown in Figure 4, macroscopic cracks were observed in both samples at 2 separate locations perpendicular to the build direction as shown in Figure 6. An optical micrograph of cylinder 8 along the build (Z) direction in Figure 7 confirms the presence of cracking perpendicular to the build direction alongside a near fully dense cylinder otherwise as observed in XCT results of Figure 4. Cylinder 5 (transition mode) which had a density of 99.97% is also visualized through optical micrographs along the XY plane and the Z direction in Figure 7, thereby confirming the presence of close to no porous defects in the core and subsurface regions as shown by XCT results in Figure 4 and Figure 5. Cracking during LPBF of Ti-6242Si has not been reported in the previous two studies targeting LPBF of Ti-6242Si [5,18]. Observed cracking during LPBF of Ti-6242Si could be potentially attributed to excessive shrinkage and higher residual stress in keyhole mode as reported by Song et al. for LPBF of Ti64 [35]. There is also a possibility of hydrogen induced embrittlement causing cracks in the martensitic microstructure as observed by Silverstein and Eliezer during LPBF of Ti64 [36]. Additionally, subsolidus cracking during the arc welding of Ti-6211, an alpha-beta Ti alloy, was observed to be caused by poor hot ductility of the martensitic alpha-prime (α′) microstructure by Damkroger et al. [37]. Bowden and Starke [38] had previously found that Ti-6211 structures with a larger prior beta grain size were more susceptible to a high-temperature ductility loss than were samples with a smaller prior beta grain size, but Damkroger et al. [37] found the opposite to be true. These hypothesis for cracking origins during LPBF of Ti-6242Si will be evaluated as part of future work. Additionally, future work would also involve a reprinting of conduction and transition mode coupons to check the repeatability of the successful process parameters from this work in obtaining near fully dense crack free Ti-6242Si samples.

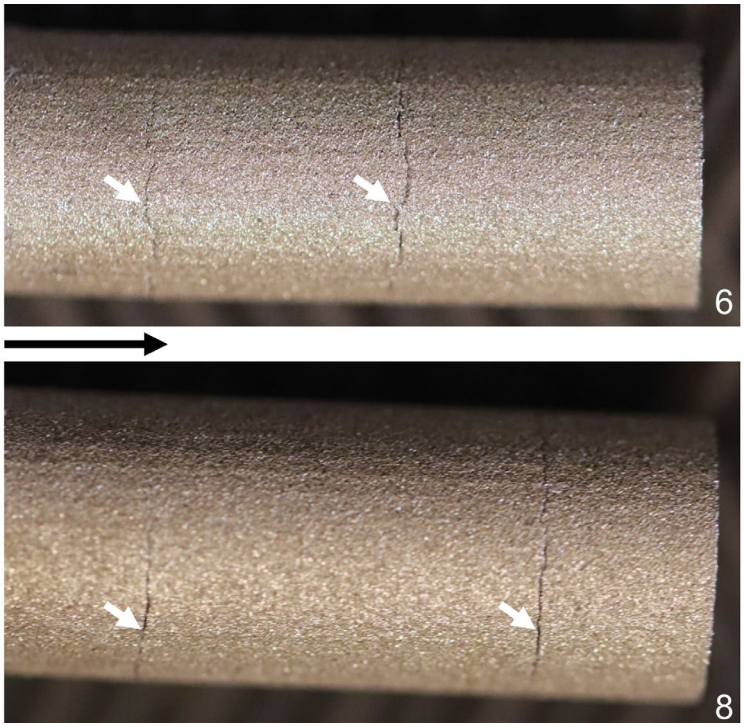

Figure 6. Macroscopic cracking (white arrows) observed in cylinders 6 and 8 from Print 1, which are predicted to have keyhole mode core process parameters as per Figure 2. Build (Z) direction is given by the black arrow.

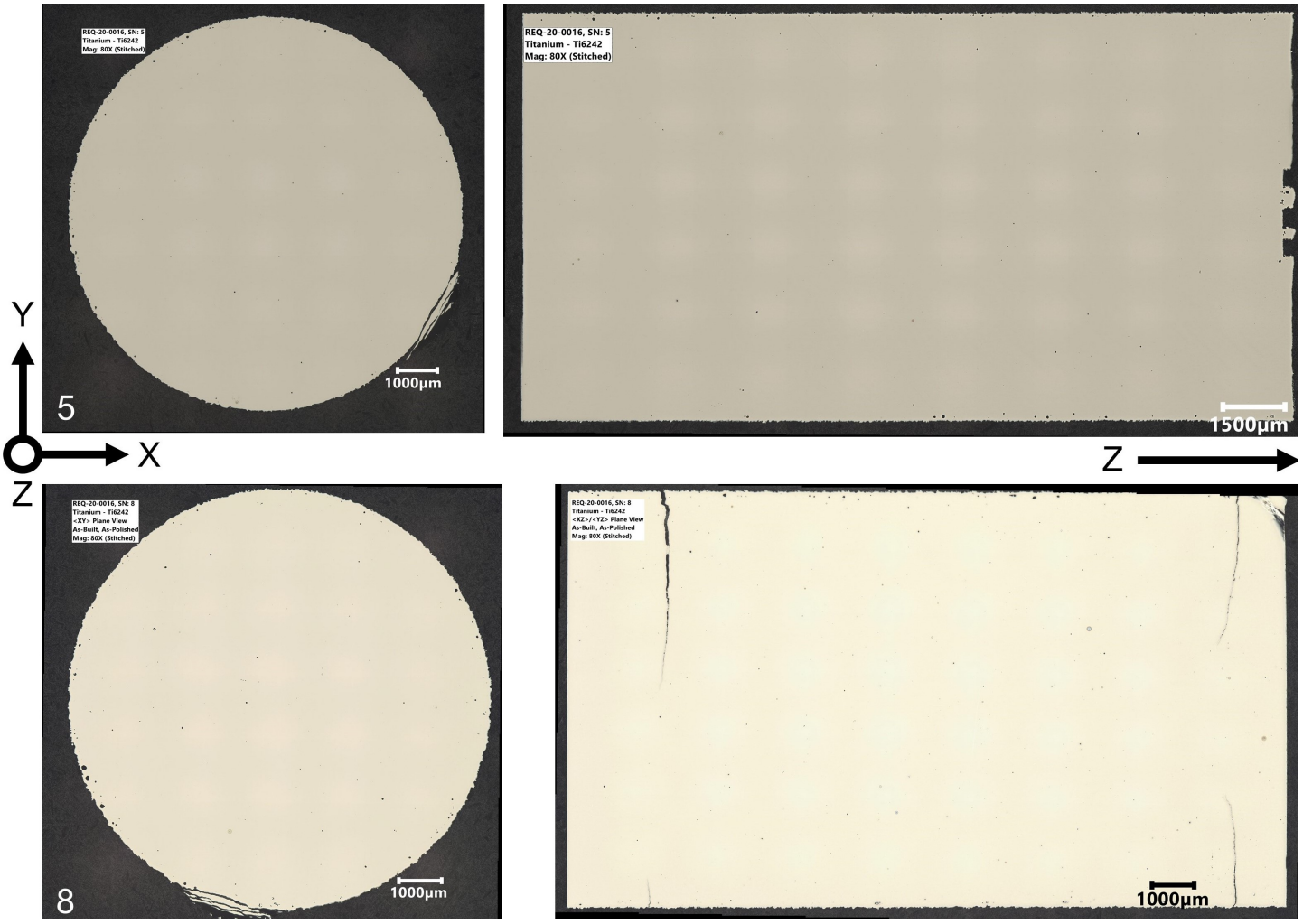

Figure 7. Optical micrographs of cylinder 5 (transition mode) and cylinder 8 (keyhole mode) along the XY plane and the build (Z) direction.

Side-skin surface characteristics

An evaluation of the effects of LPBF process parameters for the border scan such as laser power and scan speed (by virtue of exposure time) showcases a trend towards reduced surface roughness (*Sa* and *Sz*) in the keyhole melting mode in Figure 3. These findings are similar to results by Patel et al. [22] during LPBF of Ti64, where a preliminary investigation into the effects of border LPBF process parameters lead to *Sa* values of 9.05 ± 0.37 µm with transition/keyhole mode process parameters compared to 17.05 ± 1.59 µm for conduction mode process parameters. Figure 8 showcases a significantly reduced impact of balling and adhered partially fused powder particles on the side-skin surface of Ti-6242Si cuboids in the transition and keyhole mode LPBF process parameters, when compared to the conduction mode process parameters. The lowest surface roughness (*Sa* and *Sz*) values in Figure 3 were observed in the keyhole mode samples which could be associated to the effects of powder denudation caused by the increasing extent of vaporization shown by Matthews et al. [39], leading to lower side-skin surface roughness during LPBF [22], confirmed by Figure 8. It must be noted that studying the effect of core LPBF process parameters or studying the interaction of core and border process parameters on side-skin surface roughness of Ti-6242Si was outside the scope of this work. Care must be taken to understand the extent to which the border parameters in keyhole melting mode may detrimentally contribute to sub-surface porosity and elevated edges. Subsurface porosity will lead to a reduction in the fatigue life of a given part [21], while elevated edges can lead to the powder recoater hitting the edges of a given sample thereby disturbing the flow of powder on the LPBF build plate, and can also lead to recoater blade damage [22].

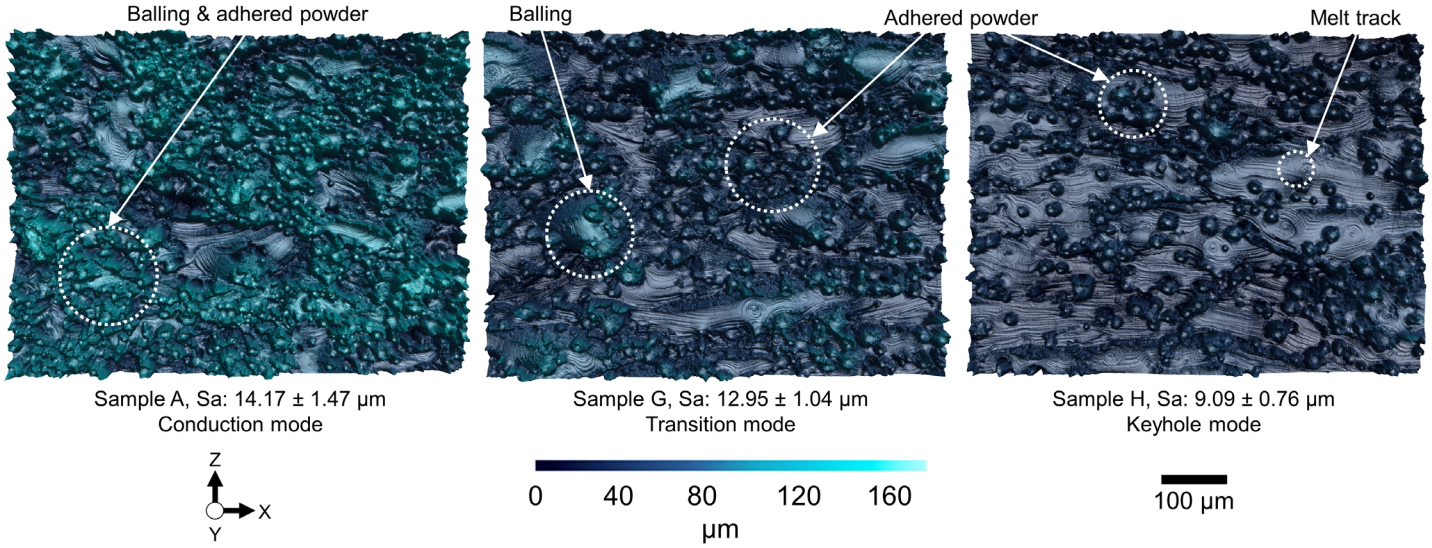

Figure 8. A three-dimensional height map representation of side-skin surface characteristics along with *Sa* values for sample A (conduction mode), sample G (transition mode), sample H (keyhole mode).

Conclusions

This work involved the use of process diagrams and a temperature prediction for investigating the effect of LPBF process parameters including laser power, scan speed, and beam spot radius on the density and side-skin surface roughness of Ti-6242Si, a near-alpha titanium alloy. The key findings are summarized below:

1. Normalized processing diagrams and X-ray computed tomography show that Ti-6242Si has a broad process window with parts above 99.90% density observed in conduction, transition, and keyhole melting modes of LPBF. The overall density range obtained was 99.55-99.98 %. The highest density parts (up to 99.98 %) are observed in the transition melting mode for Ti-6242Si, with reduced number of defects in both the core and subsurface regions.

2. Subsurface porous defects are the main contributor towards porosity across all melting modes for LPBF of Ti-6242Si. These defects are caused by rapid formation and collapse of deep vaporized regions due to the lower laser beam velocity at the turn points of a given layer, which is common across most LPBF

systems. Simulations in this work predicted vaporization for all of the LPBF process parameters used, leading to the prevalence of subsurface defects in all samples.

3. Keyhole mode LPBF of Ti-6242Si leads to macroscopic cracking perpendicular to the build direction, which will be investigated as part of future work.

4. Keyhole mode LPBF process parameters for border scans of Ti-6242Si leads to a side-skin surface roughness, *Sa*, values of less than 10 μm, which is the lowest roughness value when compared to transition and conduction mode LPBF process parameters. This reduction is associated to reduced effects of adhered partially fused powder particles and balling on the side-skin surfaces of Ti-6242Si.

Acknowledgments

The authors appreciate the funding support received from Federal Economic Development Agency for Southern Ontario (FedDev Ontario, grant # 814654). We acknowledge the generous donation of the powder from AP&C, QC, Canada and for their support in this project. The authors would also like to thank Hamid Azizi and Mehrnaz Salarian from Burloak Technologies for their inputs and help with metallography of the samples. In addition, the authors would like to acknowledge the help of Henry Ma, Jerry Ratthapakdee, James Farnsworth, and Karl Rautenberg in helping with the deployment and characterization of builds at the MSAM Group in the University of Waterloo.

References

[1] D. Küpper, W. Heising, G. Corman, M. Wolfgang, C. Knizek, V. Lukic, Get ready for industrialized additive manufacturing, Boston Consulting Group, 2017.
[2] A. Salmi, F. Calignano, M. Galati, E. Atzeni, An integrated design methodology for components produced by laser powder bed fusion (L-PBF) process, Virtual and Physical Prototyping. 13 (2018) 191–202.
[3] P.C. Priarone, V. Lunetto, E. Atzeni, A. Salmi, Laser powder bed fusion (L-PBF) additive manufacturing: On the correlation between design choices and process sustainability, Procedia CIRP. 78 (2018) 85–90. https://doi.org/10.1016/j.procir.2018.09.058.
[4] B. Dutta, F. Froes, Additive manufacturing of titanium alloys: state of the art, challenges and opportunities, Butterworth-Heinemann, 2016.
[5] C. Fleißner-Rieger, T. Pfeifer, T. Jörg, T. Kremmer, M. Brabetz, H. Clemens, S. Mayer, Selective Laser Melting of a Near-α Ti6242S Alloy for High-Performance Automotive Parts, Advanced Engineering Materials. n/a (2020) 2001194. https://doi.org/10.1002/adem.202001194.
[6] Z. Liu, B. He, T. Lyu, Y. Zou, A Review on Additive manufacturing of titanium alloys for aerospace applications: directed energy deposition and beyond Ti-6Al-4V, JOM. (2021) 1–15.
[7] B. Jackson, Norsk Titanium to Deliver the World's First FAA-Approved, 3D-Printed, Structural Titanium Components to Boeing, Norsk Titanium. (2017). https://www.norsktitanium.com/media/press/norsk-titanium-to-deliver-the-worlds-first-faa-approved-3d-printed-structural-titanium-components-to-boeing (accessed June 4, 2021).
[8] M. Wang, X. Lin, W. Huang, Laser additive manufacture of titanium alloys, Materials Technology. 31 (2016) 90–97.
[9] J. Avila, S. Bose, A. Bandyopadhyay, Additive manufacturing of titanium and titanium alloys for biomedical applications, in: Titanium in Medical and Dental Applications, Elsevier, 2018: pp. 325–343.
[10] Y.-L. Hao, S.-J. Li, R. Yang, Biomedical titanium alloys and their additive manufacturing, Rare Metals. 35 (2016) 661–671.
[11] S. Singh, S. Ramakrishna, Biomedical applications of additive manufacturing: Present and future, Current Opinion in Biomedical Engineering. 2 (2017) 105–115. https://doi.org/10.1016/j.cobme.2017.05.006.
[12] M. McGregor, S. Patel, S. McLachlin, M. Vlasea, Architectural bone parameters and the relationship to titanium lattice design for powder bed fusion additive manufacturing, Additive Manufacturing. (2021).

[13] K.-H. Richter, S. Orban, S. Nowotny, Laser cladding of the titanium alloy Ti6242 to restore damaged blades, in: LIA, 2004: p. 1506.
[14] V.M. Tabie, C. Li, W. Saifu, J. Li, X. Xu, Mechanical properties of near alpha titanium alloys for high-temperature applications-a review, Aircraft Engineering and Aerospace Technology. (2020).
[15] G. Welsch, R. Boyer, E. Collings, Materials properties handbook: titanium alloys, ASM international, 1993.
[16] G.E. Totten, D.S. MacKenzie, 25.1 The Titanium Atom, in: ASM Handbook Volume 4E - Heat Treating of Nonferrous Alloys, ASM International, 2016. https://app.knovel.com/hotlink/pdf/id:kt011ODJ52/asm-handbook-volume-4e/the-titanium-atom.
[17] F.J. Ridgeon, M.J. Raine, D. Halliday, M. Lakrimi, A. Thomas, D.P. Hampshire, Superconducting Properties of Titanium Alloys (Ti-64 and Ti-6242) for Critical Current Barrels, IEEE Transactions on Applied Superconductivity. 27 (2016) 1–5.
[18] H. Fan, S. Yang, Effects of direct aging on near-alpha Ti–6Al–2Sn–4Zr–2Mo (Ti-6242) titanium alloy fabricated by selective laser melting (SLM), Materials Science and Engineering: A. 788 (2020) 139533.
[19] P.A. Hooper, Melt pool temperature and cooling rates in laser powder bed fusion, Additive Manufacturing. 22 (2018) 548–559. https://doi.org/10.1016/j.addma.2018.05.032.
[20] S. Ly, A.M. Rubenchik, S.A. Khairallah, G. Guss, M.J. Matthews, Metal vapor micro-jet controls material redistribution in laser powder bed fusion additive manufacturing, Scientific Reports. 7 (2017) 4085. https://doi.org/10.1038/s41598-017-04237-z.
[21] S. Patel, H. Chen, M. Vlasea, Y. Zou, The influence of divergent laser beams on the laser powder bed fusion of a high reflectivity aluminium alloy, ArXiv:2105.07920 [Cond-Mat, Physics:Physics]. (2021). http://arxiv.org/abs/2105.07920 (accessed June 4, 2021).
[22] S. Patel, A. Rogalsky, M. Vlasea, Towards understanding side-skin surface characteristics in laser powder bed fusion, Journal of Materials Research. 35 (2020) 2055–2064. https://doi.org/10.1557/jmr.2020.125.
[23] A. Rogalsky, I. Rishmawi, L. Brock, M. Vlasea, Low cost irregular feed stock for laser powder bed fusion, Journal of Manufacturing Processes. 35 (2018) 446–456. https://doi.org/10.1016/j.jmapro.2018.08.032.
[24] J.C. Ion, H.R. Shercliff, M.F. Ashby, Diagrams for laser materials processing, Acta Metallurgica et Materialia. 40 (1992) 1539–1551.
[25] M. Thomas, G.J. Baxter, I. Todd, Normalised model-based processing diagrams for additive layer manufacture of engineering alloys, Acta Materialia. 108 (2016) 26–35.
[26] J. Ye, S.A. Khairallah, A.M. Rubenchik, M.F. Crumb, G. Guss, J. Belak, M.J. Matthews, Energy Coupling Mechanisms and Scaling Behavior Associated with Laser Powder Bed Fusion Additive Manufacturing, Advanced Engineering Materials. 21 (2019) 1900185. https://doi.org/10.1002/adem.201900185.
[27] D. Dai, D. Gu, Effect of metal vaporization behavior on keyhole-mode surface morphology of selective laser melted composites using different protective atmospheres, Applied Surface Science. 355 (2015) 310–319. https://doi.org/10.1016/j.apsusc.2015.07.044.
[28] S. Patel, M. Vlasea, Melting mode thresholds in laser powder bed fusion and their application towards process parameter development, in: Proceedings of the 20th Annual International Solid Freeform Fabrication Symposium, Austin, TX, 2019: pp. 1190–1199.
[29] A. Khorasani, I. Gibson, U.S. Awan, A. Ghaderi, The effect of SLM process parameters on density, hardness, tensile strength and surface quality of Ti-6Al-4V, Additive Manufacturing. 25 (2019) 176–186. https://doi.org/10.1016/j.addma.2018.09.002.
[30] Y. (Morris) Wang, C. Kamath, T. Voisin, Z. Li, A processing diagram for high-density Ti-6Al-4V by selective laser melting, Rapid Prototyping Journal. 24 (2018) 1469–1478. https://doi.org/10.1108/RPJ-11-2017-0228.
[31] T. Voisin, N.P. Calta, S.A. Khairallah, J.B. Forien, L. Balogh, R.W. Cunningham, A.D. Rollett, Y.M. Wang, Defects-dictated tensile properties of selective laser melted Ti-6Al-4V, Mat. Des. 158 (2018) 113–126. https://doi.org/10.1016/j.matdes.2018.08.004.

[32] C. Kamath, Determination of Process Parameters for High-Density, Ti-6Al-4V Parts Using Additive Manufacturing, Lawrence Livermore National Lab. (LLNL), Livermore, CA (United States), 2017. https://doi.org/10.2172/1413166.
[33] J.J.S. Dilip, S. Zhang, C. Teng, K. Zeng, C. Robinson, D. Pal, B. Stucker, Influence of processing parameters on the evolution of melt pool, porosity, and microstructures in Ti-6Al-4V alloy parts fabricated by selective laser melting, Progress in Additive Manufacturing. 2 (2017) 157–167. https://doi.org/10.1007/s40964-017-0030-2.
[34] H. Gong, H. Gu, K. Zeng, J. j. s Dilip, D. Pal, B. Stucker, D. Christiansen, J. Beuth, J. Lewandowski, Melt Pool Characterization for Selective Laser Melting of Ti-6Al-4V Pre-alloyed Powder, in: Proceedings of 15th Annual International Solid Freeform Fabrication Symposium, Austin, TX, 2014.
[35] B. Song, S. Dong, B. Zhang, H. Liao, C. Coddet, Effects of processing parameters on microstructure and mechanical property of selective laser melted Ti6Al4V, Materials & Design. 35 (2012) 120–125. https://doi.org/10.1016/j.matdes.2011.09.051.
[36] R. Silverstein, D. Eliezer, Hydrogen trapping in 3D-printed (additive manufactured) Ti-6Al-4V, Materials Characterization. 144 (2018) 297–304. https://doi.org/10.1016/j.matchar.2018.07.029.
[37] B. Damkroger, G. Edwards, B. Rath, Investigation of subsolidus weld cracking in alpha-beta titanium alloys, Welding Journal. 68 (1989) 290–302.
[38] D.M. Bowden, E. Starke, The effect of microstructure and deformation behavior on the hot ductility of Ti-6Al-2Nb-1Ta-0.8 Mo, Metallurgical Transactions A. 15 (1984) 1687–1698.
[39] M.J. Matthews, G. Guss, S.A. Khairallah, A.M. Rubenchik, P.J. Depond, W.E. King, Denudation of metal powder layers in laser powder bed fusion processes, Acta Materialia. 114 (2016) 33–42. https://doi.org/10.1016/j.actamat.2016.05.017.